Defect-directed growth of symmetrically branched metal nanocrystals

RESEARCH ARTICLE

Defect-Directed Growth of Symmetrically Branched Metal Nanocrystals

Joshua D. Smith,[a] Eva Bladt,[b] Joseph A. C. Burkhart,[a] Naomi Winckelmans,[b] Kallum M. Koczkur,[a] Hannah M. Ashberry,[a] Sara Bals,*[b] and Sara E. Skrabalak*[a]

Abstract: Branched plasmonic nanocrystals (NCs) have attracted much attention due to electric field enhancements at their tips. Seeded growth provides routes to NCs with defined branching patterns and, in turn, near-field distributions with defined symmetries. Here, a systematic analysis was undertaken in which seeds containing different distributions of planar defects were used to grow branched NCs in order to understand how their distributions direct the branching. Characterization of the products by multimode electron tomography and analysis of the NC morphologies at different overgrowth stages indicate that the branching patterns are directed by the seed defects, with the emergence of branches from the seed faces consistent with minimizing volumetric strain energy at the expense of surface energy. These results contrast with growth of branched NCs from single-crystalline seeds and provide a new paradigm for the synthesis of symmetrically branched plasmonic NCs.

Introduction

Plasmonic nanocrystals (NCs) provide new opportunities for security devices, biological sensors, heterogeneous catalysis, photothermal therapeutics, and plasmon-enhanced spectroscopies.[1] The diversity of applications arises from the tunable localized surface plasmon resonances (LSPRs) of plasmonic NCs. By changing their size, shape, composition, and environment, the extinction (scattering + absorbance) spectrum and electric field (EF) enhancements of NCs can be engineered for specific applications.[2] Recently, branched plasmonic NCs have received attention in spectroscopy and sensing because EF enhancements are localized at their tips.[3] For example, molecules adsorbed preferentially at the tips of Au nanostars are predicted to experience Raman signal enhancements ten orders of magnitude greater than that of molecules adsorbed to their polyhedral cores.[4] Given that the optoelectronic properties of plasmonic NCs are shape dependent, structures with well-defined branching patterns are needed. Recently, branched metal NCs with defined symmetries were obtained by seed-mediated growth methods.[5] Much of this work has focused on the overgrowth from single-crystalline seeds in which the studies led to the following paradigm: branch growth initiates and proceeds from the high-energy vertices of shape-controlled seeds under kinetically controlled growth conditions ($k_{metal\ addition} > k_{metal\ adatom\ diffusion}$).[5] In this study, we demonstrate that this paradigm is insufficient to describe the synthesis of branched metal NCs from shape-controlled seeds with planar defects, where branch growth proceeds from seed faces instead of seed vertices.

NCs with planar defects (*e.g.,* twin planes and stacking faults) provide unique symmetries not readily available from single-crystalline face-centered cubic (fcc) metals.[6a, 6b] That is, such NCs are not confined by the cubic symmetry of the lattice and can be synthesized as decahedra, plates, icosahedra, and other shapes by acquiring strain.[6] For example, five-fold twinned decahedra of a fcc metal can be prepared from five single crystal tetrahedral sub-units, which are connected by twin boundaries.[7] This configuration leaves a gap of 7.35°, which is compensated by introducing bond elongation at the interfaces (*i.e.,* strain).[7] Similarly, fcc metal icosahedra undergo lattice deformations to account for 6% empty space that arises from their 20 single crystal tetrahedral sub-units.[8] Such strain can be significant enough to initiate relief mechanisms such as surface roughening, anisotropic growth as well as the introduction of dislocations, re-entrant grooves, and grain boundaries.[8,9] For example, José-Yacaman and co-workers found, by aberration-corrected scanning transmission electron microscopy (STEM), that decahedra with 300 nm edge lengths contain dislocations to stabilize the structures.[10] High index facets were identified on all sides of the decahedra, highlighting how unique surface energy landscapes can be introduced through the balance of surface energy and volumetric strain energy.[10]

Here, the growth of branched NCs from seeds with different planar defect distributions is reported in order to understand how these defects contribute to the emergence of branched NCs with new symmetries. In contrast to single-crystalline seeds, branch growth proceeds from the faces of defect-rich seeds. Structural characterization of the branched NCs coupled with mechanistic studies reveal that the final NC morphologies are consistent with balancing surface energy and volumetric strain energy during growth, giving a more complete perspective on how branched NCs with defined symmetries can be synthesized.[6a,8, 11]

Results and Discussion

Au icosahedra, decahedra, pentatwinned rods, and triangular plates were used as seeds with seed-mediated co-reduction (SMCR) to investigate the influence of planar defects in the synthesis of branched NCs. SMCR is a robust route to symmetrically branched NCs from single-crystalline seeds of different shapes.

[a] J. Smith, J. Burkhart, Dr. K. Koczkur, H. Ashberry, Prof. S. Skrabalak
Department of Chemistry
Indiana University - Bloomington
800 E. Kirkwood Ave, Bloomington, Indiana 47405, (United States)
E-mail:
[b] Dr. E Bladt, Dr. N. Winckelmans, Prof. S. Bals
EMAT
University of Antwerp
Groenenborgerlaan, 171, B – 2020 Antwerp (Belgium)

Supporting information for this article is given via a link at the end of the document.

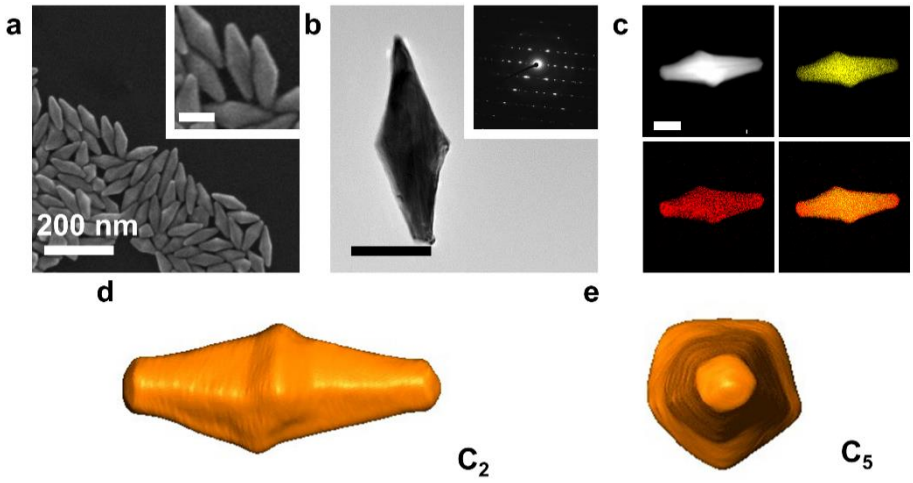

Figure 1. Products from SMCR onto small pentatwinned rods. Bipyramids were characterized by (a), SEM TEM with inset SAED (b), STEM-EDS (c) with Au (yellow), Pd (red), and mixed mapping, and 3D visualization of the HAADF-STEM reconstruction viewed from the d, C_2 and e, C_5 axes. Unless noted, all scale bars are 50 nm.

Here, Au and Pd precursors are co-reduced by L-ascorbic acid in the presence of hexadecyltrimethylammonium bromide (CTAB) and sodium salicylate as capping agents. Previous studies of SMCR using single-crystalline seeds, such as cubes, octahedra, tetrahedra, and single-crystal rods, has led to the following paradigm: the symmetry of the seeds dictates the symmetry of the branched NCs and that branch growth proceeds from the vertices of the seeds.[5c] This universality of branched NC formation was anticipated to hold when growing from seeds with different planar defect distributions, with the general synthetic approach summarized in Figure S1. Here, we note that introduction of Pd to the largely Au structures gives multifunctionality and improves branch NC stability compared to all-Au overgrowth while providing a kinetic lever to access branched NCs during the growth process (Au $k_{\text{metal adatom diffusion}}$ > Pd $k_{\text{metal adatom diffusion}}$).[5, 12]

The seeds were analyzed prior to SMCR by scanning electron microscopy (SEM) and transmission electron microscopy (TEM) (Figure S2), and their structural features are summarized in Table S1. Products were characterized by SEM, TEM, selected-area electron diffraction (SAED), powder X-ray diffraction (PXRD), multimode electron tomography (ET), and high-angle annular dark field (HAADF) STEM coupled with energy dispersive X-ray spectroscopy (EDS).

When small pentatwinned rods (SEM measurements: width 16 ± 4 nm, length 49 ± 4 nm) with an aspect ratio of 3.1 were used as seeds (Figure S2a), bipyramidal structures were grown by SMCR (Figure 1a) in 94.7% yield. SEM images reveal that the bipyramids are almost double in width (33 ± 2 nm) and length (103 ± 7 nm) compared to the initial seeds. The inset of Figure 1b shows the SAED pattern obtained along the C_2 axis of a bipyramid and agrees with what has been previously observed for pentatwinned Au bipyramids.[13] As indicated by elemental mapping (Figure 1c) and PXRD (Figure S3), Pd and Au are incorporated as alloys in the bipyramid structures. These results are in good agreement with previous work.[5c, e] To better understand the final structure of the bipyramids, a 3D reconstruction of a single nanoparticle was obtained using HAADF-STEM tomography. The symmetry transfer of the pentatwinned rods (D_{5h}) to the bipyramids is evident from the reconstructed particle presented in Figure 1 d,e and Supplemental Video 1.

In contrast, larger pentatwinned rods (Figure S2b; SEM measurements: width 57 ± 4 nm, length 82 ± 4 nm) with an aspect ratio of 1.6 gave rise to NCs with 10 branches, in which one branch extends from each {111} facet at the ends of the pentatwinned rods (Figure 2). SEM reveals that the NCs are larger after SMCR, with widths of 114 ± 15 nm and lengths of 167 ± 11 nm, and the D_{5h} symmetry of the seeds is conserved in the final product. Overall, all products are branched with 47.1% clearly displaying 10 branches and D_{5h} symmetry (with other structures arising from seed impurities). STEM-EDS and PXRD further confirms the co-deposition of Au and Pd (Figure 2c, Figure S3). The twin planes of the seeds do not propagate through the branches as no characteristic contrast difference is evident in the branches from high magnification TEM imaging (Figure S4), and this structural characteristic is further supported by the tomographic analysis in Figure 2b (inset), d, and e. The twin planes in Figure 2d (in purple) clearly do not propagate through the branches of the NC.

Although NC reconstructions from HAADF-STEM provide the highest shape accuracy, diffraction contrast of planar defects is severely limited.[14] Inversely, low-angle annular dark field STEM

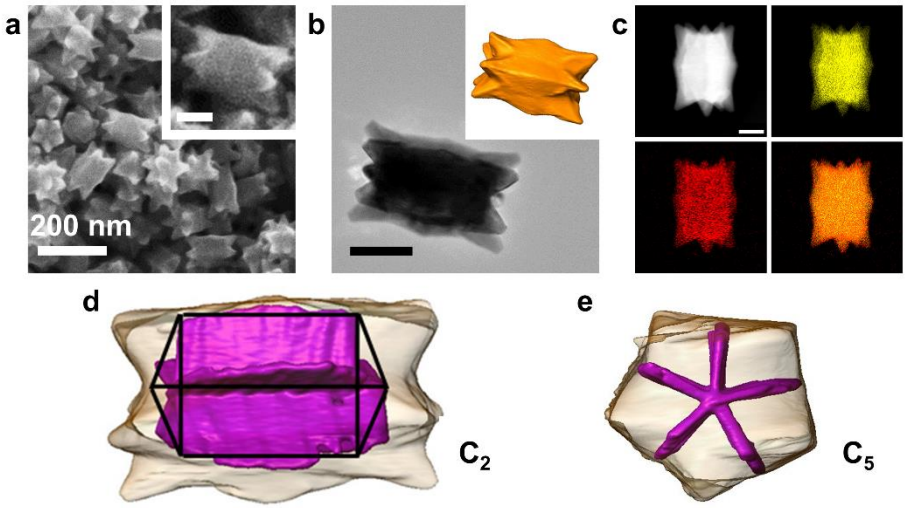

Figure 2. Products from SMCR onto large pentatwinned rods characterized by (a), SEM (b), TEM with inset HAADF-STEM reconstruction (b), STEM-EDS (c) with Au (yellow), Pd (red), and mixed mapping, and 3D visualization of superimposed HAADF and LAADF reconstructions of the d, C_2 and e) C_5 axes. Unless noted, all scale bars are 50 nm.

(LAADF-STEM) provides high diffraction contrast of the planar defects but at the expense of shape accuracy.[14] Here, multimode ET of the branched pentatwinned rods was performed in which HAADF-STEM and LAADF-STEM tilt series were acquired simultaneously. Thereby, both the morphology of the NC and the location of present twin planes can be reconstructed in an accurate manner. Superimposed reconstructions are presented in Figure 2d,e and Supplemental Video 2. This analysis reveals that branch growth proceeds from each {111} facet terminating the rod ends, without planar defects extending into the branches.

This structural analysis supports that planar defects are guiding the symmetry of branching. Regardless of the dimensions of the pentatwinned rod seeds, NCs with D_{5h} symmetry and 5-fold twin planes are observed after overgrowth. Interestingly, the dimensions of the initial seed dictate the final NC morphology. Seeded overgrowth from small pentatwinned rods has been studied in an all-Au system by Liz-Marzán and co-workers, where the rods expanded into truncated decahedra, with bipyramids identified as an intermediate product.[15] They proposed that growth from the higher energy {100} facets of the rods was favored, resulting in bipyramidal structures with {113} facets expressed along the length of the structures.[15] We note that this intermediate structure and our bipyramids are consistent with limited lateral growth, which should minimize volumetric strain energy relative to surface energy and the expression of high index facets. When larger rods are used as seeds, branch growth is observed. Since the initial size of the large pentatwinned rods is almost double of the size of the smaller pentatwinned rods (*i.e.,* the volumetric strain energy is much greater), different overgrowth behavior is reasonable. Notably, branching is consistent with minimization of volumetric strain energy, and this outcome will be discussed in full shortly.

Decahedra (TEM measurements: widths 62 ± 2 nm, lengths 76 ± 3 nm) with widths similar to the large rods were used as seeds (Figure S2c) and yielded 10-branched NCs after SMCR (Figure 3) at 62.1%. The product is similar to those grown from large pentatwinned rods, but shorter, and maintain the D_{5h} symmetry of the seeds. TEM and ET reconstructions viewed along the C_2 and C_5 rotational axes confirm preservation of the multiply twinned interior and branches that proceed from the {111} facets of the decahedral seeds (Figure 3b,d, Supplemental Video 3, and Figure S5). STEM-EDS and PXRD supports Au/Pd alloy formation (Figure 3c, Figure S3). As observed with pentawinned rods, the branches proceed from the {111} facets of the decahedral seeds. This finding further supports that the seed symmetry is translated to the final structure and overgrowth is directed by the defect distribution of the seeds. Similar to growth from the large pentatwinned rods, multimode ET reveals that the twin planes of the decahedral seeds increase in width (61 ± 1 nm to 109 ± 7 nm) and length (76 ± 3 nm to lengths of 121 ± 3 nm).

The structural analysis of branched NCs from large pentatwinned rods and decahedra indicates that a similar overgrowth pathway is occurring. When comparing the large pentatwinned rods to decahedral seeds, the size and dimensions of the twins increase in both overgrown NCs. Thus, we propose that seeds reach a critical size prior to the

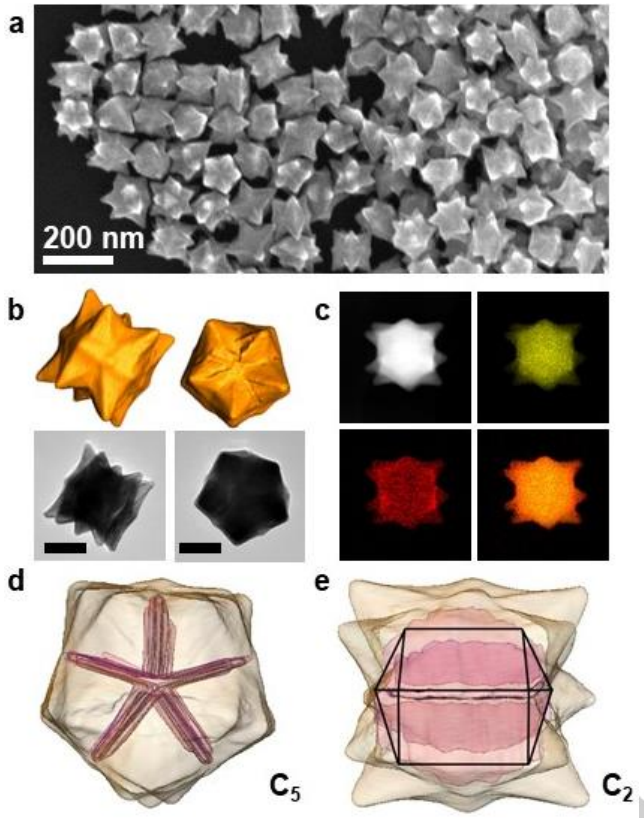

Figure 3. Branched decahedra obtained from SMCR onto decahedral seeds were characterized by (a) SEM, (b) TEMs with inset HAADF-STEM reconstructions, (c) STEM-EDS with Au (yellow), Pd (red), and mixed mapping, and 3D visualization of superimposed HAADF and LAADF reconstructions of the (d), C_2 and (e), C_5 axes. Unless noted, all scale bars are 50 nm.

initiation of branch growth, with the branches emerging to minimize the total NC energy by minimizing the volumetric strain energy.

When considering branch growth from defect-rich seeds, the total free energy of the particle (G(T)) must be considered. Previous work by Marks and Olvera de la Cruz on the elastic strain energy effects in faceted NCs found that the G(T) of multiply twinned NCs can be approximated using Equation 1:

$$G(T) \approx V\left(W_V^D + \Delta\bar{G}_f\right) + \sum_i A_i(\gamma_i + W_{Si}) + \gamma_t A_t \qquad (1)$$

where V is the NC volume, W_V^D is the per-volume strain energy, $\Delta\bar{G}_f$ is the change in free energy per unit volume, A is the surface area, W_S is the surface strain energy, and γ is the surface energy.[8,9b,15] The subscript *i* and *t* subscripts refer to certain facets and the twin boundary, respectively.[9b,16] Their finite element analysis revealed that a balance between surface energy and volumetric strain energy accounts for different decahedral shapes at different particle sizes.[11a] At smaller sizes, W_V^D of the NC is small, and the free energy is dominated by the surface energy term, favoring convex decahedra. As the particle increases in size, W_V^D continues to increase as a function of a^3, with star shapes becoming favored.[11a] This analysis indicates that the free energy of the twinned NCs is a balancing act between surface energy and volumetric strain energy.

Applying this model to our system, at a critical size, the volumetric strain energy will dominate over the surface energy of the NC. At this point, the introduction of branches would be favored because the energy penalty for branch formation is lower than that for increasing the twin plane dimensions. The simulations by Marks and Olvera de la Cruz also revealed that the surfaces of the decahedra display highest stress and strain energy densities at the face-centers of the five tetrahedral segments as well as the center of the outer edges (not at the twin boundaries).[11a] This distribution is supported by measurements of lattice strain in Au nanodecahedra by atomic resolution TEM.[16] These studies support the emergence of branches from the face-centers rather than the equatorial vertices or twin boundaries.

To better understand the competition between branch formation (i.e., surface energy) and strain energy, a time study was conducted in which bis(*p*-suflonatophenyl)phenylphopsphine dihydrate dipotassium salt (BSPP) was introduced to quench the growth from decahedra at time points between 10 seconds and 1 hour.[17] Results of the time study are presented in Figure 4, in which the products from the reaction aliquots were analyzed by SEM. The widths of the particles increase from 43 ± 4 nm initially to 48 ± 5 nm within 10 seconds (Figure 4a) and 57 ± 6 nm within 1 minute (Figure 4c). The increase in particle width is accompanied by particle elongation from 37 ± 5 nm at 10 seconds (Figure 4a) to 59 ± 4 nm within 1 minute (Figure 4c). Longer reaction times only increased the dimensions slightly, while the total number of particles with obvious branching and D_{5h} symmetry observable by SEM increases with reaction time (Figure 4d,e). ET analysis of the NCs after 10 and 30 seconds (Figure S6 and Figure S7) is consistent with the dimensional analysis by SEM but also reveals that, by 30 seconds, all the decahedral seeds have grown to structures with tiny branches not evident by SEM (Figure S7). Interestingly, at 10 seconds, the particles have increased in size from the initial seed dimensions

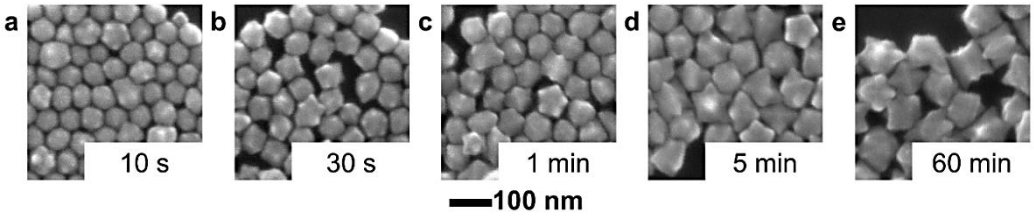

f

Sample	Length (nm)	Width (nm)	Branched NCs
a	37 ± 5	48 ± 5	2.1%
b	41 ± 4	56 ± 4	5.4%
c	59 ± 4	57 ± 6	11.3%
d	70 ± 7	62 ± 5	14.6%
e	79 ± 6	67 ± 6	16.2%

Figure 4. Decahedral nanoparticles were analyzed by SEM at times of (a) 10 seconds, (b) 30 seconds, (c) 1 minute, (d) 5 minutes, and (e) 60 minutes. Quantitative analysis of the time study is presented in (f) table below.

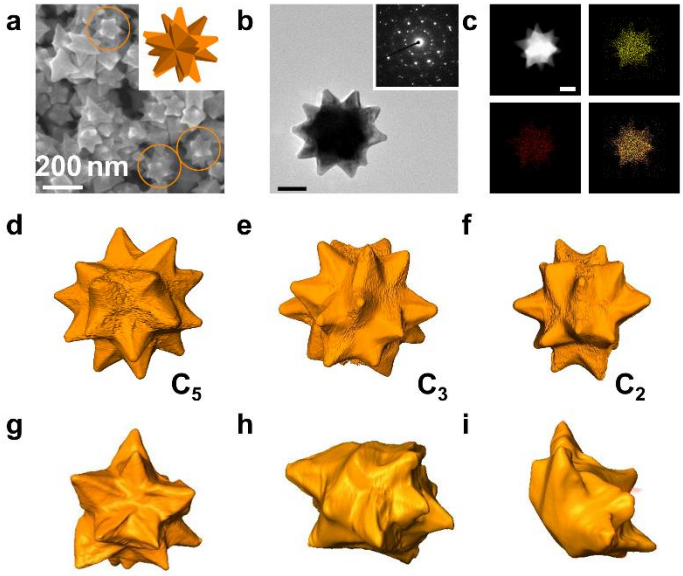

Figure 5. Branched icosahedra were characterized by (a) SEM and model, (b) TEM with inset SAED, and (c) STEM-EDS of side and top with Au (yellow), Pd (red), and mixed mapping, 3D visualization HAADF reconstruction of a 20 branched icosahedra near its (d) C_5, (e), C_3, (f) and C_2 axes, and (g-i) 3D visualization HAADF reconstructions of branched icosahedra grown from imperfect seeds. Unless noted, all scale bars are 50 nm.

of 43 ± 4 nm, with a mixed population of non-branched and short-branched structures observed (Figure 4a and Figure S6).

A representative non-branched NC (Figure S6a, b) has a width of 58 nm and length of 46 nm, while a representative branched NC (Figure S6e, f) is larger, with a width of 68 nm and length of 58 nm. Microscopy analysis of ~20 particles reveals that the smaller NCs show no obvious branching while the larger NCs have small branches. We attribute this observation to there being a critical NC size before branching initiates and proceeds in <111> directions. We note that the critical size refers to the point at which volumetric strain becomes large and the formation of branches becomes more favorable. Like small pentatwinned rods, different overgrowth from small decahedral seeds is expected since the

initial volumetric strain is less. Indeed, similar bipyramid structures are observed when growing from small decahedral seeds with 26 ± 4 nm diameters (Figure S8). These analyses are consistent with an exchange between volumetric strain energy and the increase in surface energy from branch growth.

As branches grow from the {111} facets of pentatwinned seeds, we anticipated that 20-branched NCs with I_h symmetry would be produced by SMCR using icosahedral Au seeds (Figure S2d). This hypothesis is based on idealized icosahedra having 15 twin planes and 20 {111} facets from which branches could grow. In fact, all-Au 20 branched NCs with I_h symmetry were reported by Lu and co-workers when growing from such seeds; however, their work did not analyze structure formation within the context of the capping effects of alkylamines.[18a] Here, highly branched NCs are produced (98.3% yield) with SMCR when icosahedral seeds are used, as shown in Figure 5. A complex SAED pattern is obtained from analysis of an individual particle and agrees with what has been previously observed for icosahedral Au NCs (Figure 5b).[18] STEM-EDS in Figure 5c and PXRD in Figure S3 indicates Au/Pd alloy formation. Since a perfect icosahedron has 20 {111} facets, 20-branched NCs would be expected, with an example presented in Figure 5d-f and Supplemental Video 4. However, branched NCs that preserve the perfect I_h symmetry are a minor product (8.9% yield).

ET analysis of additional particles shows that many branched NCs are produced in high yield with branches proceeding from the {111} facets of the seeds, but the total number of branches varied between 10 and 20. See Figure 5g-i and Supplemental Videos 5-7 for examples. To understand the origin of this symmetry reduction in the final branched NCs, tomographic analysis of the icosahedral seeds was performed (Figure S7). Seeds with nearly perfect I_h symmetry and uniform facets were observed (Figure S9a, b, d, f) in addition to less perfect seeds with slightly deformed facets (Figure S9c, e). These slight variations from one icosahedral seed to the next can account for the variations in branched NCs and why perfectly branched icosahedra are only found in 8.9% yield. This finding suggests that there is a minimum facet area to facilitate branching, much as there is a dependence with rod and decahedra sizes. Significantly, the twin planes present within the icosahedral seeds do not extend into the branches (Figure S10), supporting that branch growth proceeds to limit the expansion of planar defects.[8,10,19]

Finally, triangular nanoplates with stacking faults were used as seeds (Figure S2e, f) for the growth of branched NCs by SMCR (Figure 6). The smallest plates (edge length: 35 ± 5 nm, width: 21 ± 6 nm) produced NCs with two branches, one from the top and one from the bottom of a given nanoplate (Figure 6a,b,

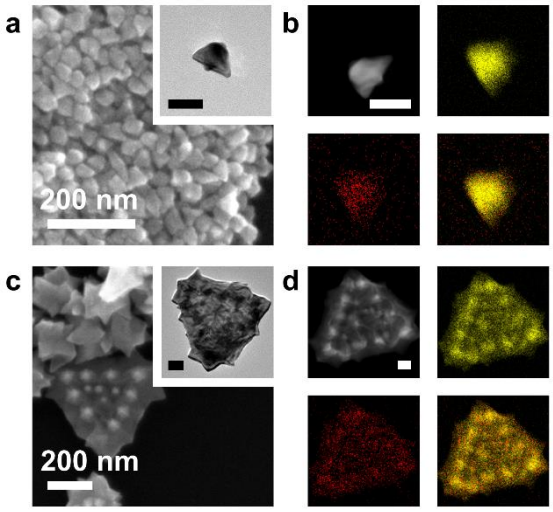

Figure 6. Branched nanoplates obtained from SMCR onto triangular plates. Single branched and multi-branched structures were characterized by (a,c) SEM with inset TEM, (b,d) and STEM-EDS with Au (yellow), Pd (red), and mixed mapping, respectively. Unless noted, all scale bars are 50 nm.

Figure S11, and 3D visualization HAADF reconstruction in Supplemental Video 8). The structures have edge lengths of 58 ± 9 nm and widths of 83 ± 13 nm and were present in 79.3% yield. When triangular plates with edge lengths of 350 ± 21 nm (approximately 8.2% yield and in a mixture of smaller plates and polyhedra) were used as seeds, multibranched structures were observed, in which nearly periodic branch growth is evident as well as Au and Pd deposition (Figure 6c,d and Figure S3). SAED in Figure S12 indicates that the NCs are crystalline. After overgrowth, the edge lengths of the NCs are 397 ± 28 nm, indicating that branches are growing from the {111} facets of the nanoplates in a manner similar to what was observed with smaller nanoplates as seeds.

Several mechanisms have been cited for periodic overgrowth. Millstone and co-workers proposed that supramolecular assemblies of CTAB behave as templates for linear growth of Pt islands on gold triangular prisms.[20] However, such a mechanism is unlikely in our system as the higher CTAB concentration promotes uniform surface coverage. Also, the distance between each row of islands templated by CTAB (5.1 ± 0.8 nm)[20] is much smaller than the spacing observed from the nearly periodic branched nanoplates here (55 ± 16 nm). Alternatively, nearly periodic overgrowth has been explained by well-ordered dislocation networks.[21] Kern and co-workers demonstrated that a Pt substrate with periodic strain-relief patterns can template well-defined Ag islands on its surface.[22] A similar strain relief mechanism may be occurring with overgrowth from large plates, but differences between bulk surfaces and nanoscale dimensions must be considered.

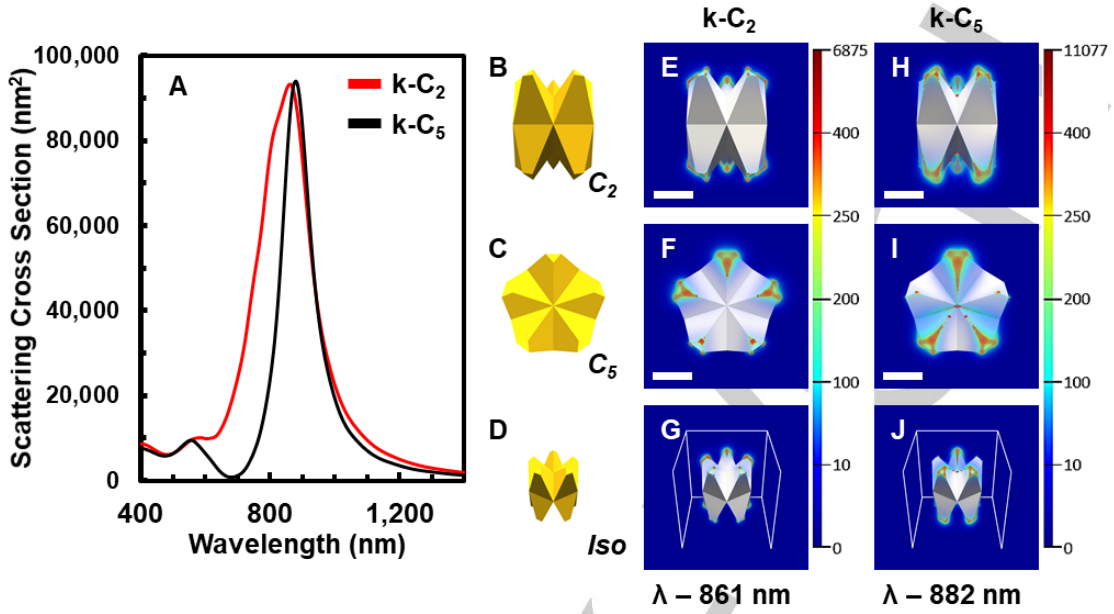

Figure 7. Finite-difference time domain calculation of unpolarized (a) scattering cross sections for the k-C_2 (red) and k-C_5 (black) injection axis of branched decahedra, (b-d) models of the C_2, C_5, isometirc orientation of a branched decahedra, and near-field distributions for *k-C₂* (e-g, λ_{max} = 861 nm) and *k-C₅* (h-j, λ_{max} = 882 nm) injection axes. Scale bars are 50 nm and the white boxes in (g) and (j) have side lengths of 200 nm.

The branched plasmonic NCs reported here provide new opportunities for many applications but a better understanding of their plasmonic behavior is required.[1] As shown in Figure S13, the branched NCs display broad LSPR peaks in the visible-NIR spectral range. Here, finite-difference time domain (FDTD) simulations were used to investigate far- and near-field behavior of these structures. The plasmonic behavior of a branched decahedron is presented in Figure 7, with a branched pentatwinned rod and a branched icosahedron being analyzed in Figures S14 and S15, respectively. Branched decahedron, pentatwinned rod, and icosahedron models were constructed using the geometrical dimensions of the synthesized structures; however, the models were treated as all-Au NCs due to limitations in simulating complex Au/Pd distributions.[24,25] The simulations of all-Au NC provide a qualitative analysis of EF behavior of the synthesized branched NCs. The LSPR features from the symmetry of the branched NCs are maintained, but the LSPR peaks occur at different energies with respect to their experimental analogues. [24,25]

The far-field (Figure 7a) and near-field (Figure 7e-j) plasmonic behavior was analyzed by changing the light's injection axis, *k*, along the C_2 and C_5 rotational axis of the branched decahedron (Figure S16).[3d,26] Figure 7 reveals that the branched decahedron displays three major LSPR peaks: a longitudinal LSPR between 861-882 nm, a transverse LSPR at 809 nm, and an equatorial LSPR between 556-587 nm. Interestingly, branched decahedra grow anisotropically to widths of 109 ± 7 nm and lengths of 121 ± 3 nm. This anisotropic growth results in a longitudinal resonance that occurs from tips on opposite C_5 axes and a transverse resonance that occurs between the branches on the same C_5 axis. The absence of a shoulder for *k-C₅* spectra in Figure 7a further supports the assignment of the two LSPR resonances since the excitation of the transverse LSPR is impossible.[3d, 26] The peak at 556-587 nm is attributed to the resonance along the equatorial plane.[27] Similarly, the branched pentatwinned rod displays longitudinal, transverse, and equatorial resonances but at different LSPR energies (Figure S14). In contrast, the branched icosahedron displays a single LSPR resonance due to its isotropic structure (Figure S15). The measured absorbance spectrum of branched NCs display broad single LSPRs (Figure S13 and Figure S17). This difference is attributed to the bimetallic compositions and the mixed morphological yields of branched NCs.

When considering the near-field behavior of the branched decahedron, areas of strong EF enhancements are found at the tips (Figure 7e-j). The increased EF intensity localized at the tips (Figure 7e-j) is expected.[3d] Tip-localized EF enhancement is also observed for the branched pentatwinned rod (Figure S14) and branched icosahedron (Figure S15). Interestingly, bimetallic branched NCs display large refractive index sensitivities (RIS).[24,28] Here, the change in LSPR position for branched decahedra was monitored as a function of the RI for the dispersing media (Figure S17). Amazingly, Figure S18 shows that branched decahedra display one of the highest RIS and figure of merits (FOM) for NCs that have LSPR ≤ 900 nm (RIS: 503, FOM: 2.31).[24]

Conclusion

The branching symmetries as a function of seed shape are summarized in Table S2. In sharp contrast to single-crystalline NCs, branch growth occurs from the faces of seeds rich with planar defects. This is a new paradigm for branched NC growth. Our analysis attributes that branch growth proceeds in a manner which minimizes the build-up of additional strain energy. Seeds with planar defects provide unique energy landscapes compared to single-crystalline seeds, opening new pathways toward branched NCs with new symmetries. We note, however, that this trend may be different with different growth conditions or with different metallic seeds as the energetics of twin formation, volumetric strain, and surface energy depend on both composition and surface passivation.[23] More broadly, initial seed symmetry is translated to the final branched NCs regardless of whether overgrowth proceeds from seed vertices or facets, providing general guidelines for how structures with specific optical properties and near-field distributions can be achieved by design. Optoelectronic investigations reveal the NCs synthesized here provide new platforms for many different applications.

Experimental Section

Complete details of chemicals, protocols, analytical techniques, and computational parameters can be found in the Supplemental Information.

Acknowledgements

The authors thank Samantha Harvey for her initial observations of branched structures, Alexander Chen for his help with SAED, the staff of the Nanoscale Characterization Facility (Dr. Yi Yi),Electron Microscopy Center (Dr. David Morgan and Dr. Barry Stein), and Molecular Strucre Center at Indiana University. J.S. recognizes a fellowship provided by the Indiana Space Grant Consortium. E. B. acknowledges a post-doctoral grant from the Research Foundation Flanders (FWO, Belgium). This project has received funding from the National Science Foundation (award number: 1602476), Research Corporation for Scietific Advancement (2017 Frontiers in Research Excellence and Discovery Award), and the European Union's Horizon 2020 research and innovation program under grant agreement No 731019 (EUSMI) and No 815128 (REALNANO).

Keywords: Nanoparticles • Plasmon • Crystal Growth • Alloys • Strain

[1] a) A. Smith, P. Patton, S. Skrabalak, *Adv. Funct. Mater.* **2016**, *126*, 1315-1321.; b) X. Huang, P. Jain, I. El-Sayed, M. El-Sayed, *Lasers Med. Sci.* **2008**, *23*, 217.; c) J. Anker, W. Hall, O. Lyanders, N. Shah, J. Zhao, R. Van Duyne, *Nat. Mater.* **2008**, *7* 442-453.; d) Q. Yang, H. Jiang, *Chem. Soc. Rev.* **2017**, *46*, 4774-4804.; e) K. Willets, R. Van Dune, *Annu. Rev. Phys. Chem.* **2007**, *58*, 267-297.; f) K. Mayer, J. Hafner, *Chem. Rev.* **2011**, *111*, 3828-3857.

[2] a) A. Bansal, J. Sekhon, S. Verma, *Plasmonics* **2014**, *9*, 143-150.; b) I. Sosa, C. Noguez, R. Barrera, *J. Phys. Chem. B* **2003**, *107*, 6269-6275.; c) K. Kelly, E. Coronado, L. Zhao, G. Schatz, *J. Phys. Chem. B* **2003**, *107*, 668-677.

[3] a) F. Hao, C. Nehl, J. Hafner, P. Nordlander, *Nano Lett.* **2007**, *7*, 729-732.; b) L. Rodríguez-Lorenzo, R. Álvarez-Puebla, F. de Abajo, L. Liz-Marzán, *J. Phys. Chem. C* **2010**, *114*, 7336-7340.; c) S. Dondapati, T. Sau, C. Hrelescu, T. Klar, F. Stefani, J. Feldmann, *ACS Nano* **2010**, *4*, 6318-6322.; d) J. Smith, Z. Woessner, S. Skrabalak, *J. Phys. Chem. C* **2019**, *123*, 18113-18123.; e) E. Ringe, M. Langille, K. Sohn, J. Zhang, J. Huang, C. Mirkin, R. Van Duyne, L. Marks, *J. Phys. Chem. Lett.* **2012**, *3*, 1479-1483.; f) X. Xia, S. Xie, M. Liu, H. Peng, J. Wang, M. Kim, Y. Xia, *PNAS* **2013**, *110*, 6669-6673.

[4] P. Kumar, I. Pastoriza-Santos, B. Rodríguez-González, F. de Abajo, L. Liz-Marzán, *Nanotechnology* **2008**, *19*, 015606.;

[5] a) Y. Xia, K. Gilroy, H. Peng, X. Xia, *Angew. Chem. Int. Ed.* **2017**, *56*, 60-95.; *Angew. Chem.* **2017**, *129*, 60-98.; b) B. Lim, Y. Xia, *Angew. Chem. In. Ed.* **2011**, *50*, 76-85.; *Angew. Chem.* **2011**, *123*, 78-87.; c) R. Weiner, M. Kunz, S. Skrabalak, *Acc. Chem. Res.* **2015**, *48*, 2688-2695.; d) Y. Xiong, Y. Ma, J. Li, J. Huang, Y. Yan, H. Zhang, J. Wu, D. Yang, *Nanoscale* **2017**, *9*, 11077-11084; e) C. DeSantis, A. Peverly, D. Peters, S. Skrabalak, *Nano Lett.* **2011**, 2164-2168; f) C. DeSantis, A. Sue, A. Radmilovic, H. Liu, Y. Losovyj, S. Skrabalak, *Nano Lett.* **2014**, *14*, 4145-4150.

[6] a) K. Gilroy, H. Peng, X. Yang, A. Ruditskiy, Y. Xia, *Chem. Commun.* **2017**, *53*, 4530-4541.; b) X. Xia, Y. Xia, *Nano Lett.* **2012**, *12*, 6038-8042.; c) Y. Xia, X. Xia, H. Peng, *J. Am. Chem. Soc.* **2015**, *137*, 7947-7966.; d) Y. Xia, Y. Xiong, B. Lim, S. Skrabalak, *Angew. Chem. Int. Ed.* **2009**, *48*, 60-103.; *Angew. Chem.* **2008**, *121*, 62-108.

[7] C. Johnson, E. Tnoeck, M. Ezcurdie, B. Rodríguez-González, I. Pastoriza-Santo, L. Liz-Marzán, M. Hÿtch. *Nat. Mater.* **2008**, *7*, 120-124.

[8] L. Marks, L. Peng, *J. Phys. Condes. Matter.* **2016**, *28*, 053001.

[9] a) S. Patala, L. Marks, M. Olvera de la Cruz, *J. Phys. Chem. Lett.* **2013**, *4*, 3089-3094.; b) S. Narasimhan, D. Vanderbilt, *Phys. Rev. Lett.* **1992**, *69*, 15641567.; c) M. Van Hove, R. Koestner, P. Stair, J. Bibérian, L. Kesmodel, I. Bartoš, G. Somorjai, *Surf. Sci.* **1981**, *103*, 189-217.

[10] G. Casillas, J. Velázques-Salazar, M. Jose-Yacaman, *J. Phys. Chem. C* **2012**, *116*, 8844-8848.

[11] a) S. Patala, L. Marks, M. Olver de la Cruz, *J. Phys. Chemc. C* **2013**, *117*, 1485-1494.; b) A. Chen, M. Scanlan, S. Skrabalak, *ACS Nano* **2017**, *11*, 12624-12631.; c) H. Brune, K. Bromann, H. Röder, K. Kern, *Phys. Rev. B* **1995**, *52*, 14380-14383.

[12] a) W. Albrecht, E, Bladtm H. Vanrompay, J. Smith, S. Skrabalak, S. Bals, *ACS Nano* **2019**, *13*, 6522-6530.; b) A. Taylor, A. Siddiquee, J. Chon, *ACS Nano* **2014**, *8*, 12071-12079. c) L. Zhang, Z. Xie, J. Gong, *Chem. Soc. Rev.* **2016**,*45*, 3916-3934.

[13] A. Sánchez-Iglesias, N. Winckelmans, T. Altantzis, S. Bals, M. Grzelczak, L. Liz-Marzán, *J. Am. Chem. Soc.* **2017**, *139*, 107-110.

[14] N. Winckelmans, T. Altantzis, M. Grzelczak, A. Sánchez-Iglesias, L. Liz-Marzán, S. Bals, *J. Phys. Chem. C* **2018**, 171, 13522-13528.

[15] E. Carbó-Argibay, B. Rodrígues-González, I. Pastoriza-Santos, J. Pérez-Juste, L. Liz-Marzán, *Nanoscale* **2010**, *2*, 2377-2383.

[16] a) M. Walsh, K. Yoshida, A. Kuwabra, M. Pay, P. Gai, E. Boyes, *Nano Lett.* **2012**, *12*, 2027-2031. b) B. Goris, J. De Beenhouwer, A. De Backer, D. Zanaga, K. Joost Batenburg, A. Sánches-Iglesias, L. Liz-Marzán, S. Van Aert. S. Bals, J. Sijbers, G. Van Tendeloo, *Nano Lett.* **2015**, *15*, 6996-7001.

[17] a) R. Weiner, C. DeSantis, M. Cardoso, S. Skrabalak, *ACS Nano.* **2014**, *8*, 8625-8635.; b) J. Zhang, M. Langille, C. Mirkin, *J. Am. Chem. Soc.* **2010**, *132*, 12502-12510.

[18] a) W. Niu, Y. Chua, W. Zhang, H. Huang, X. Lu, *J. Am. Chem. Soc.* **2015**, *137*, 10460-10463.; b) M. Langille, J. Zhang, M. Personick, C. Mirkin, *Science* **2012**, *337*, 954-957.

[19] A. Barnard, N. Young, A. Kirkland, M. van Huis, H. Xu, *ACS Nano.* **2009**, *3*, 1431-1436.

[20] a) P. Straney, L. Marbella, C. Andolina, N. Nuhfer, J. Millstone, *J. Am. Chem. Soc.* **2014**, *136*, 7873-7876.; b) P. Straney, N. Diemler, A. Smith, Z. Eddinger, M. Gilliam, J. Millstone, *Langmuir* **2018**, *34*, 1084-1091.

[21] a) C. Ozkan, W. Nix, H. Gao, *J. Matter. Res.* **1999**, *14*, 3247-3256.; b) G. Grochola, I. Snook, S. Russo, *Mol. Simul.* **2016**, *42*, 484-493.; c) H. Gao, W. Nix, **1999**, *29*, 173-209.

[22] H. Brune, M. Giovannini, K. Bromann, K. Kern, *Nature* **1998**, *394*, 451-453.

[23] a) M. King, M. Personick, *Nanoscale* **2017**, *9*, 17914-17921; b) T. Bian, H. Zhang, Y. Jiang, C, Jin, J. Wu, H. Yang, D. Yang, *Nano Lett.* **2015**, *15*, 7808-7815.; c) X. Wang, M. Vara, M. Luo, H. Huang, A. Ruditskiy, J. Park, S. Bao, J. Liu, J. Howe, M. Chi, Z. Xie, Y. Xia, *J. Am. Chem. Soc.* **2015**, *137*, 15036-15042.

[24] a) A. Smith, S. Harvey, S. Skrabalak, R. Weiner, *Nanoscale* **2016**, *8*, 16841-16845.; e) C. DeSantis, S. Skrabalak, *Langmuir* **2012**, *28*, 9055-9062.

[25] X. Zhu, Z. Zhuo, Q. Li, Z. Yang, J. Wang, *Adv. Funct. Mater*. **2016**, *26*, 341-352.

[26] A. Smith, R. Weiner, S. Skrabalak. *J. Phys. Chem. C* **2016**, *120*, 20563-20571.

[27] J. RodrÍgues-Fernádez, C. Novo, V. Myroshnychenko, A. Funston, A. Sánchez-Iglesias, I. Pastoriza-Santos, J. Pérez-Juste, J. GarcÍa de Abajo, L. Liz-Marzán, P. Mulvaney, *J. Phys. Chem. C* **2009**, *113*, 18623-18631.

[28] H. Chen, X. Kou, Z. Yang, J. Wang, *Langmuir* **2008**, *24*, 5233-5273.

Entry for the Table of Contents

RESEARCH ARTICLE

Branched metal nanocrystals are exciting platforms in many applications. Here, we present a new seeded-growth paradigm where branches extend from the faces of defect-rich seeds and, thus, revealing that the evolution of defect-rich seeds to branched structures is a balancing act between surface energy and volumetric strain energy

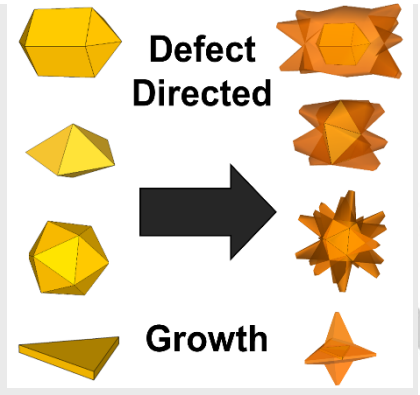

Joshua D. Smith, Eva Bladt, Naomi Winckelmans, Joseph A. C. Burkhart, Kallum M. Koczkur, Hannah M. Ashberry, Sara Bals and Sara E. Skrabalak**

Page No. – Page No.

Defect-Directed Growth of Symmetrically Branched Metal Nanocrystals